Journal of Animal & Plant Sciences, 35(4): 2025, Page: 1037-1049
ISSN (print): 1018-7081; ISSN (online): 2309-8694
https://doi.org/10.36899/JAPS.2025.4.0088

IN VIVO MAGNETIC RESONANCE IMAGING OF TUBERCULOUS MENINGITIS RAT MODEL USING NEAR-INFRARED LONG-PERSISTENT LUMINESCENT NANOMATERIALS

X.Y. Li[1] and L.Y.Z. Huang[2*]

[1]Department of Tuberculosis, The First Hospital of Changsha, Changsha, 410005, Hunan, China;
[2]Department of Neurology, The First Hospital of Changsha, Changsha, 410005, Hunan, China.

*Corresponding author's email: huangliying1688@126.com

ABSTRACT

'This research was aimed to explore the adoption value of near-infrared (NIR) long-persistent luminescent nanomaterials for *in vivo*magnetic resonance imaging (MRI) of tuberculous meningitis in rat model. Firstly, NIR long-persistent luminescent nanomaterials were synthesized using the sol-gel methodology. The materials were thoroughly evaluated using X-ray diffraction, characterization techniques, fluorescence spectroscopy, and property analysis, with investigations into the effects of different thermal treatment temperatures.A tuberculous meningitis rat model was established in five rats (experimental group), while other five rats were injected with saline (control group). The successful establishment of the model was confirmed through hematoxylin-eosin (HE) staining. The remaining rats from each group were selected for further analysis($ZnGa_2O_4:Cr^{3+}$NIR group and saline group). The prepared $ZnGa_2O_4:Cr^{3+}$NIR solution was injected into $ZnGa_2O_4:Cr^{3+}$NIR group, while saline was injected into saline group. The effects of these injections on NIR imaging and their impact on MRI were subsequently analyzed.The synthesized $ZnGa_2O_4:Cr^{3+}$ nanomaterials exhibited uniform particle sizes ranging from 40 to 80 nm, with a NIR emission peak at 709 nm. The afterglow decay curve demonstrated an initial rapid decay followed by stabilization, with the optimal excitation time determined to be 15 minutes. Histopathological analysis confirmed the successful establishment of rat model, with experimental group showing significantly higher inflammatory cell counts (48.3 ± 6.7 vs. 16.2 ± 1.5 cells/field, $P<0.05$) and histological scores (3.7 ± 0.5 *vs.* 0.5 ± 0.3, $P<0.05$) compared to control group. After injection of nanomaterials, MRI signal intensity in experimental group was significantly enhanced, with the signal-to-noise ratio increasing from 4.5 ± 0.8 to 8.2 ± 1.2 ($P<0.05$) and the contrast-to-noise ratio rising from 1.9 ± 0.4 to 3.5 ± 0.6 ($P<0.05$). Additionally, the ventricular area in the experimental group was approximately 15% smaller than that of control group (0.38 ± 0.05 cm^2*vs.* 0.45 ± 0.06cm^2, $P<0.05$).*In vivo*MRI imaging based on NIR long-persistent luminescent nanomaterials showed a good application potential for the research of tuberculous meningitis rat model.

Keywords: near-infrared long-persistent luminescent nanomaterials; tuberculous meningitis; animal model; *in vivo* magnetic resonance imaging

Published first online June 10, 2025 Published final July 29, 2025

INTRODUCTION

Tuberculous meningitis is a central nervous system infection caused by *Mycobacterium tuberculosis* (Fukushima *et al.*, 2023). It progresses rapidly and can lead to severe neurological damage and irreversible impairment (Manyelo*et al.*, 2021). Its diagnosis mainly relies on medical history, clinical symptoms, cerebrospinal fluid examination, and imaging techniques (Méchaï and Bouchaud, 2019). Due to the lack of specificity in the clinical manifestations of tuberculous meningitis, existing diagnostic methods have certain limitations in early detection, such as low sensitivity or insufficient specificity, which may lead to missed or incorrect diagnoses (Bystritsky and Chow, 2022; Dian *et al.,* 2020).

Magnetic resonance imaging (MRI) *in vivo* imaging technology is a non-invasive medical imaging technique (Biegger *et al.*, 2020). Compared to X-ray and computed tomography (CT), *in vivo*MRI offers higher resolution and contrast, providing more detailed and accurate information (Zhang and Liang, 2019; Liu *et al.*, 2021). MRI has been confirmed to be effective in evaluating the brain tissue structure and function in mouse models (Iannucci *et al.*, 2024). Fluorescence sensors demonstrate advantages such as visualization, rapid detection, simplicity of operation, and high sensitivity (Zhang *et al.*, 2022; Jacob *et al.*, 2022). In a

study, researchers injected the ovalbumin-Alexa Fluor 555tracer into the cerebrospinal fluid to create an immunologic formulation, and observed through real-time vascular MRI technology that it could reveal the three-dimensional anatomical structure of the meningeal lymphatic vessels (Jacob *et al.*, 2022). Long-persistent luminescent nanomaterials, also known as persistent luminescent nanomaterials, can emit light for an extended period even after the cessation of excitation. They exhibit renewable luminescence and do not require re-excitation, making them widely used in the preparation of optical materials for sensing and non-spontaneous fluorescence detection (Chen *et al.*, 2019). Near-infrared (NIR) long-persistent luminescent nanomaterials are a class of nanomaterials with excellent luminescent properties and biocompatibility, showing promising potential for adoptions in the field of biomedical imaging (Ge *et al.*, 2019; Jiang *et al.*, 2019; Saeboe*et al.*, 2021). Therefore, persistent luminescence nanomaterials have shown great potential in biomedical research, including applications in *in vivo* imaging, drug delivery, biosensing, and optical materials. These applications provide researchers with novel tools and methods for achieving high-resolution, long-term biological imaging and monitoring (Mahata *et al.,* 2021; Zhao *et al.,* 2021). In the context of MRI, contrast agents (such as gadolinium or iron oxide nanoparticles) are commonly employed to enhance image contrast and facilitate the visualization of specific biological processes or pathological changes(Mekonnen *et al.*, 2019). Long-persistent luminescent nanomaterials can be designed as labeling agents for MRI contrast agents to provide additional luminescent signals. This dual-modal (MRI and fluorescence) imaging approach can enhance the detection and localization capability of specific tissues or cells (Yang *et al.*, 2022). A study developed an MRI-based hybrid imaging method to analyze the biodistribution of Alexa Fluor 750-labeled immunoglobulins immunoglobulin G(IgG) and immunoglobulin A(IgA) in mice. The results revealed that MRI not only visualized the *in vivo* biodistribution characteristics of the fluorescent immunoglobulins but also clearly displayed the tissue structures of the gallbladder, thyroid, and brain (Schraven *et al.*, 2024).However, it is important to note that the application of persistent luminescence nanomaterials in medical imaging is still in the research stage, and further experimental and clinical studies are needed to evaluate their safety, stability, and performance.

Based on the aforementioned background, the objective of this research was to explore the adoption of *in vivo*MRI imaging technology based on NIR long-persistent luminescent nanomaterials in tuberculous meningitisrat model. By injecting nanomaterials into tuberculous meningitisrat modeland utilizing MRI imaging, the distribution characteristics of the materials *in vivo* were evaluated. The findings could provide new insights for the imaging diagnosis of tuberculous meningitis, offering potential auxiliary diagnostic tools.

MATERIALS AND METHODS

Fabrication of NIR luminescent long afterglow nanomaterials: The NIR long-persistent luminescent nanomaterials were synthesized using the sol-gel methodology (Clément and Mehdi, 2020), which involved three main steps: sol formation, gel formation, and preparation of nanoparticles. The specific steps were as follows:

(1) Sol formation.A dry and clean beaker was prepared, and 20.00 mL of methanol was added under ambient temperature and standard atmospheric pressure. 0.400 g of $Cr(NO_3)_3·9H_2O$ (National Pharmaceutical Group Chemical Reagents Co., Ltd., China) was weighed and added to the beaker, forming a transparent solution. Then, 0.743 g of $Zn(NO_3)_2·6H_2O$ and 1.724 g of $Ga(NO_3)_3·5H_2O$ (National Pharmaceutical Group Chemical Reagents Co., Ltd., China) were weighed and slowly added sequentially, followed by ultrasonic treatment (40 kHz, 10 min) to form a mixed solution. The $Cr(NO_3)_3·9H_2O$ solution was then added, and the mixture was stirred using a magnetic stirrer at 600 rpm for 15 min. Next, 2.011 mL of acetone (National Pharmaceutical Group Chemical Reagents Co., Ltd., China) was added, and stirring was continued for 50 min, during which the solution gradually turned light brownish-yellow. Throughout the process, the beaker was covered to prevent the solvent from evaporating too quickly. Finally, 3.986 mL of concentrated ammonia solution (25 wt%) was added drop by drop, with the addition rate controlled at 1 mL/min (to avoid violent reactions), and stirring was continued for 5 hours until the solution reached a pH of 9-10. At this point, the solution transitioned from a white colloidal state to a yellow transparent solution.

(2) Gel formation.The prepared solution was slowly heated to 80°C using a thermostatic magnetic stirrer (Shandong Bona Technology Co., Ltd., China), and stirred for 30 minutes to obtain a light-yellow gel. The resulting gel was then dried in a vacuum drying oven (Memmert, Germany) at 60°C under a vacuum of 100 Pa for 12 hours. Afterward, the dried gel was collected.

(3) Preparation of nano luminescent particles. The dried gel was ground for 10 minutes using a mortar and pestle (Shanghai Lichen Bangxi Instrument Technology Co., Ltd., China) to ensure uniform particle size. The resulting powder was then calcined in air at 400°C for 1 hour to remove residual organic materials. The calcined powder was subsequently transferred to a high-temperature sintering furnace (Jiangsu Jiuding Industrial Furnace Technology Co., Ltd., China), and heat-treated at 1,000°C for 1.5 hours under a high-purity nitrogen (99.999%) atmosphere, resulting in $ZnGa_2O_4:Cr^{3+}$NIR persistent luminescence nanophosphors. The resulting

white powder was dispersed in 5.00 mL of anhydrous ethanol and 5.00 mL of 5 mmol/L sodium hydroxide solution, followed by 40 kHz ultrasonic treatment for 15 minutes to remove residual by-products on the surface. The mixture was then centrifuged at 10,000 rpm for 10 minutes, and the supernatant was discarded. The precipitate was collected and dried to obtain the final sample—$ZnGa_2O_4:Cr^{3+}$NIR nanomaterials, which were then used for subsequent testing.

Evaluation methods of nanomaterials: (1) X-ray diffraction (XRD) analysis. The prepared nanomaterials were analyzed using an XRD analyzer (Malvern Panalytical, China) with Cu-Kα radiation source and Ni filter. The voltage intensity was set to U=50 kV, and the current intensity was I=100mA, with a scanning speed of 4°/min.

(2) Characterization analysis. A small amount of the prepared $ZnGa_2O_4:Cr^{3+}$NIR nanomaterials was placed into a beaker, and a few drops of 5 mM sodium hydroxide solution were added.The mixture was subjected to ultrasonic treatment for 30 minutes. Subsequently, a few drops of the dispersion were dropped onto a copper grid and dried under infrared light. Finally, $ZnGa_2O_4:Cr^{3+}$NIRnanomaterialswere placed in a vacuum environment and analyzed using a transmission electron microscope (TESCAN, Shanghai, China).

(3) Fluorescence spectrum analysis. Approximately 150 mg of$ZnGa_2O_4:Cr^{3+}$NIR nanomaterialswas weighed and subjected to detection using a fluorescence spectrophotometer (Shanghai Yidian Analytical Instrument Co., Ltd., China). The voltage was set to 700 V, with both the excitation and emission slits set at 5.0 nm. The wavelength scanning speed was 1,200 nm/min.

(4) Property determination. The $ZnGa_2O_4:Cr^{3+}$NIR nanomaterialswere placed in the sample chamber and exposed to 254 nm ultraviolet light for different time durations, *i.e.,* 1 min, 5 min, 10 min, 15 min, and 30 min, followed by detection using a fluorescence spectrophotometer. Before each experiment, $ZnGa_2O_4:Cr^{3+}$NIR nanomaterials required high-temperature pretreatment to remove any existing trap filling in the sample. The pretreatment method involved heating $ZnGa_2O_4:Cr^{3+}$NIR nanomaterials in a muffle furnace (Shanghai Muffle Furnace Technology Instrument Co., Ltd., China) at 350°C for 20 minutes, with a heating rate of 5°C/min.

Detection of different heat treatment temperatures on the properties of NIR luminescent nanomaterials:(1) Transmission electron microscope(TEM)observation of the morphological changes of the nanomaterials.The thermal treatment temperatures were set at 800°C, 1,000°C, and 1,200°C, respectively, (this temperature range effectively controls the crystal structure and optical properties of the material. Below 800°C, the material may fail to fully crystallize, while temperatures exceeding 1,200°C may lead to excessive sintering or morphological changes of the particles, thereby affecting their luminescent properties. Therefore, selecting these three temperature points helps to evaluate the optimal luminescent performance of the material under different heat treatment conditions), to investigate the changes in luminescent nanomaterial characterization at different temperatures. The methodology involved taking an appropriate amount of the ground $ZnGa_2O_4:Cr^{3+}$NIR nanomaterial powder and maxing it with a 5 mM sodium hydroxide solution (QuzhouBotao Chemical Co., Ltd., China). The dispersion was then treated using an ultrasonic processor (Shaanxi Kaideli Environmental Protection Technology Co., Ltd., China), and 2-3 drops of the treated solution were placed on a copper grid for morphological observation using a TEM.

(2) The changes in afterglow emission of the nanomaterials were monitored using a fluorescence spectrophotometer. The thermal treatment temperatures were set at 800°C, 1,000°C, and 1,200°C to investigate the effect of different thermal treatment temperatures on the afterglow properties of the NIR luminescent nanomaterials. The methodology involved placing an appropriate amount of the ground $ZnGa_2O_4:Cr^{3+}$NIRnanomaterialpowder in the sample chamber and exciting $ZnGa_2O_4:Cr^{3+}$NIRnanomaterialusing a 247 nm(the selection of a 247 nm excitation wavelength was based on its ability to effectively excite the long-lasting luminescent centers in the NIR luminescent nanomaterials, while minimizing phototoxic effects caused by excessive excitation, thereby ensuring optimal luminescent performance) ultraviolet lamp for 15 minutes (monitoring the afterglow emission wavelength at 621 nm). Subsequently, the afterglow decay curves of $ZnGa_2O_4:Cr^{3+}$NIRnanomaterials at different thermal treatment temperatures were monitored using a fluorescence spectrophotometer.

Establishment of animal model of tuberculous meningitis

Experimental animals: Thirteen specific pathogen-free Sprague-Dawley female rats (aged 8 weeks, weighing 250-350g; Chengdu Dashuo Experimental Animals Co., Ltd., China) were collected as experimental animals. They were housed in a specific pathogen-free negative pressure infectious animal room with a temperature of 22°C and a humidity of 55%. In the preparation of the animal model, considering that individual immune response variations among rats could potentially influence the experimental results, three rats were randomly selected for bacterial virulence recovery experiments to verify the consistency of their immune responses. The remaining ten rats were used for the main experimental procedure.Throughout the entire experimental process, the health status of the rats was

strictly monitored, and necessary immune surveillance and physiological parameter assessments were conducted to identify potential immune response variations or other abnormalities. The animal experiments strictly adhered to the guidelines for experimental procedures and ethical principles to ensure scientific validity, reliability, and respect for animal welfare. The protocols and procedures were approved by the Ethics Committee of The First Hospital of Changsha.

Virulence of standard strain H37RV in resuscitation laboratory: 1 mL of H37RV glycerol stock (Fenghui Biotechnology Co., Ltd., China) was retrieved from -80°C and inoculated into 100 mL of 7H9 medium. The culture was incubated at 37°C with shaking for 10 days until reaching the logarithmic growth phase. A 50 mL aliquot of the culture was filtered to obtain a uniform bacterial suspension, and the optical density (1 Optical Density (OD) ≈ 5 × 10^8cfu/mL) was measured and adjusted to 1 × 10^8cfu/mL. Three rats were injected intravenously with 0.2 mL of the bacterial suspension, and after 14 days, they were sacrificed. The spleens were homogenized, and the suspension was plated onto 7H10 agar plates, which were incubated at 37°C for 28 days. The colonies were selected, ground, and stored in 0.2 mL of 80% glycerol at -80°C for future use.

Fabrication of *mycobacterium tuberculosis* suspension: A 1 mL frozen H37RV glycerol bacterial suspension, which has undergone bacterial virulence recovery inside the rats at -80°C freezer, was inoculated into 100 mL of 7H9 culture medium. It was then incubated on a constant temperature shaker at 37°C for approximately 10 days until the logarithmic growth phase was reached. The culture medium was mixed thoroughly, and 30 mL of the medium was aseptically collected and centrifuged at 6,000 g/min for 10 minutes. The supernatant was discarded, and 10 mL of sterile physiological saline was applied. The mixture was resuspended by tapping. A 1 mL bacterial suspension was taken from the mixture and measured for its OD value. The bacterial concentration was calculated based on the OD value, where 1 OD was equivalent to 5E+8 cfu/mL. The bacterial suspension was diluted with sterile physiological saline to adjust the concentration to 1E+8 cfu/mL, and it was dispensed for experimental use. 1 mL of the prepared bacterial suspension was further diluted by 100 times. 0.1 mL of the diluted bacterial suspension was evenly spread on 7H10 agar plates. Five plates were inoculated and then incubated in a constant temperature incubator at 37°C for 28 days to obtain the *Mycobacterium tuberculosis* suspension.

Animals grouping: The five rats in experimental groupwere anesthetized via intraperitoneal injection of 2% sodium pentobarbital (Merck, Germany) at a dose of 40 mg/kg body weight. After 30 minutes of anesthesia, the rats' heads were fixed, and the fur around the midline of the head was shaved followed by routine iodine tincture disinfection. A central scalp incision was made to expose the anterior fontanel, and a slow intracerebral injection of 10 µL of *Mycobacterium tuberculosis* suspension (branching bacteria) was administered into the superficial projection of the lateral ventricle (0.5 mm posterior to the anterior fontanel and 1 mm lateral), at a depth of 3 mm. After the injection, the scalp was sutured with a curved triangular needle, and iodine tincture disinfection was repeated. The rats were placed in a temperature-controlled incubator to recover consciousness before being returned to their cages for one month of further care.

For the five rats in control group, the same procedure was followed, except that 10 µL of sterile physiological saline was injected into the lateral ventricle.

Modelling verification: Two rats were randomly selected from both experimental group and control group. The rats were anesthetized with 0.7% sodium pentobarbital via intraperitoneal injection at a dose of 0.01 mL/g. The rats were placed on the surgical table, and appropriate fixation devices were used to secure them, ensuring stability of their heads. An incision was made on the skin above the midline of the head with sterile surgical scissors and a blade, and the size of the incision was adjusted as needed. The skin and soft tissues were carefully pushed aside using a sterile cotton swab to expose the skull. The rats brain hemisphere was removed using fine surgical forceps and immediately fixed in 4% paraformaldehyde solution (Merck, Germany). The fixed rat brain tissue was subsequently subjected to a series of processing steps: dehydration in graded ethanol solutions, 1 hour each in 70% and 80% ethanol, 50 minutes each in 90% and 95% ethanol, 45 minutes each in absolute ethanol I and absolute ethanol II, followed by 10-15 minutes of clearing in xylene. The dehydrated tissues were embedded in routine paraffin, and the paraffin blocks were cut parallel to the longitudinal plane into continuous 4 µm thick sections, followed by slide mounting. The slides were baked at 60-65°C for 4 hours and used for Hematoxylin and Eosin (HE) staining.

HE staining was performed. The paraffin-embedded tissue blocks were taken out, and the paraffin was removed. The glass slides were consecutively immersed in xylene for dehydration (China National Pharmaceutical Group Chemical Reagent Co., Ltd., China). Then, they were fixed in 100% absolute ethanol I and absolute ethanol II. The slides were immersed in xylene for 10-15 minutes to make the tissue transparent. HE staining was performed using hematoxylin and eosin solutions (China National Pharmaceutical Group Chemical Reagent Co., Ltd., China). After staining, the tissue sections were dehydrated using a graded ethanol series and then cleared with xylene. The slides were air-

dried, mounted with a transparent mounting medium, and observed and imaged under a microscope. Inflammation cell counts were performed on HE-stained slides using *ImageJ*, and the number of inflammatory cells in five randomly selected fields was recorded. The extent of the inflammatory response was assessed using a histological scoring system (0-4 points) as detailed in Table 1. To minimize observational bias, all rat brain tissues were randomly numbered by researchers not involved in the evaluation prior to the experiment. Histological analysis was then independently performed by two experienced pathologists, who were blinded to the experimental conditions. Consistency checks were conducted on all scoring data prior to unblinding. In cases where significant discrepancies in the scoring of rat brain tissues were observed, a third evaluator was consulted to ensure the reliability of the data.

Table 1.The histological inflammation and tissue injury scoring criteria.

Score	Inflammatory cell infiltration	Vascular dilation	Tissue damage	Other pathological features
0	No inflammatory cell infiltration	None	Normal tissue structure	None
1	Few inflammatory cells (mainly around blood vessels)	Mild	Tissue structure largely intact	None
2	Moderate inflammatory cell infiltration	Obvious	Mild tissue damage	Localized vascular dilation
3	Extensive inflammatory cell infiltration	Obvious	Necrosis in tissue	Localized granuloma formation
4	Widespread inflammatory cell infiltration	Severe	Severe tissue damage	Obvious necrosis and granulomas

Evaluation of MRI imaging performance based on $ZnGa_2O_4:Cr^{3+}$NIR nanomaterials: The remaining rats were used for further MRIimagingexperiments.The prepared NIR long afterglow nanomaterials were sonicated in a certain amount of physiological saline to form a solution with a concentration of 1 mg/mL.Subsequently, $ZnGa_2O_4:Cr^{3+}$nanomaterials were excited using a handheld ultraviolet(UV) lamp with a wavelength of 254 nm, with continuous excitation for 5 minutes.One rat was randomly selected from each group and anesthetized via intraperitoneal injection of 0.7% sodium pentobarbital at a dosage of 0.01 mL/g. Subsequently, 0.05 mL of the previously excited $ZnGa_2O_4:Cr^{3+}$NIR nanomaterial solution was slowly injected into the bilateral ocular venous plexus of each rat (designated as $ZnGa_2O_4:Cr^{3+}$NIR group). Additionally, one rat was randomly selected from each group, and the nanoparticle solution was replaced with an equivalent volume of saline (designated as saline group), followed by the same treatment. The rats were then placed in an *in vivo* imaging system for signal collection and recording. The remaining one rat in each group was reserved as a backup.

Optical imaging: after the injection of nanomaterials into rats, real-time observation was conducted using an optical imaging system. The system enabled the monitoring of the dynamic changes in NIR emission and recorded the intensity variations over time.

The rat heads were scanned using a 1.5T high-field MRI system (Beckman-Kurt, USA) with a dedicated rat coil. The MRI imaging parameters were set as follows: field of view was 40 mm × 40 mm, slice thickness was 1 mm, inter-slice gap was 0.5 mm, and matrix resolution was 256 × 256. T1-weighted imaging (T1WI) was performed using a fast spin echo sequence with a repetition time of 800 ms and echo time of 12 ms. T2-weighted imaging (T2WI) was acquired using the same fast spin echo sequence, with repetition time set to 3000 ms and echo time to 80 ms. During the scanning process, the optimal imaging plane was determined based on the rat's head cross-sectional image size and diagnostic requirements, and the scanning parameters were fine-tuned to optimize image quality. To quantitatively evaluate the effectiveness of the NIRpersistent luminescence nanoparticles in MRI imaging, signal-to-noise ratio and contrast-to-noise ratio analysis methods were used. The region of interest (ROI) in the rat's brain was selected from the MRI images, and the average signal intensity of this region was compared to the background noise intensity ratio to assess image contrast and clarity. Additionally, the improvement in imaging from the nanoparticles was further analyzed by calculating the signal intensity difference between the brain region and the background area.

Statistical methods: The quantitative experimental results were presented in the format of mean ± standard deviation. All data were subjected to one-way analysis of variance (ANOVA) using SPSS 22.0 for comparison to assess statistical significance. Differences were considered statistically significant when $P<0.05$.

RESULTS

Characterization results of $ZnGa_2O_4:Cr^{3+}$NIR nanomaterials: In Figure 1A, the XRD peaks of $ZnGa_2O_4:Cr^{3+}$NIR nanomaterials are in good agreement with the standard card, with the diffraction peak positions being almost identical.The main diffraction peaks are located at 2θ ≈ 30°, 35°, 43°, 54°, 58°, and 63°, which correspond to the (220), (311), (400), (422), and (440) crystal planes of the $ZnGa_2O_4$ matrix, respectively. This indicates that the addition of Cr^{3+} did not have a notable impact on the crystal structure of the $ZnGa_2O_4$ matrix.

In Figure 1B-C, as observed by TEM, the prepared $ZnGa_2O_4:Cr^{3+}$NIR nanomaterials exhibit an irregular polygonal shape, predominantly resembling a near-circular form. The particle size ranged mainly from 40 to 80 nm, with a major peak around 60 nm, and showed good dispersibility.

The results revealed that the prepared $ZnGa_2O_4:Cr^{3+}$NIR nanomaterials exhibited a broad emission band ranging from 200 to 800 nm under UV lamp excitation.The excitation spectrum showed peaks at approximately 247 nm, 427 nm, and 553 nm, while the emission spectrum ranged from 586 to 800 nm with a peak around 709 nm (Figure 1D).

According to the fluorescence spectrum analysis in Figure 1E, the strongest excitation peak occurred at 247 nm. Hence, a 247 nm ultraviolet lamp was chosen for subsequent experiments. The decay curve monitoring results indicate that under various irradiation times, the afterglow decay curves of$ZnGa_2O_4:Cr^{3+}$NIR nanomaterials were generally consistent, showing an initial rapid decay followed by a gradual slowing down. Comparatively,$ZnGa_2O_4:Cr^{3+}$NIR nanomaterialsexhibited better NIR persistent luminescence emission ability and more similar afterglow performance when irradiated for 15 to 30 minutes. Extended excitation times may induce phototoxicity effects on biological$ZnGa_2O_4:Cr^{3+}$NIR nanomaterials. Therefore, 15 minutes was considered the optimal excitation time to achieve the best luminescence intensity without significantly affecting the biological $ZnGa_2O_4:Cr^{3+}$NIR nanomaterials

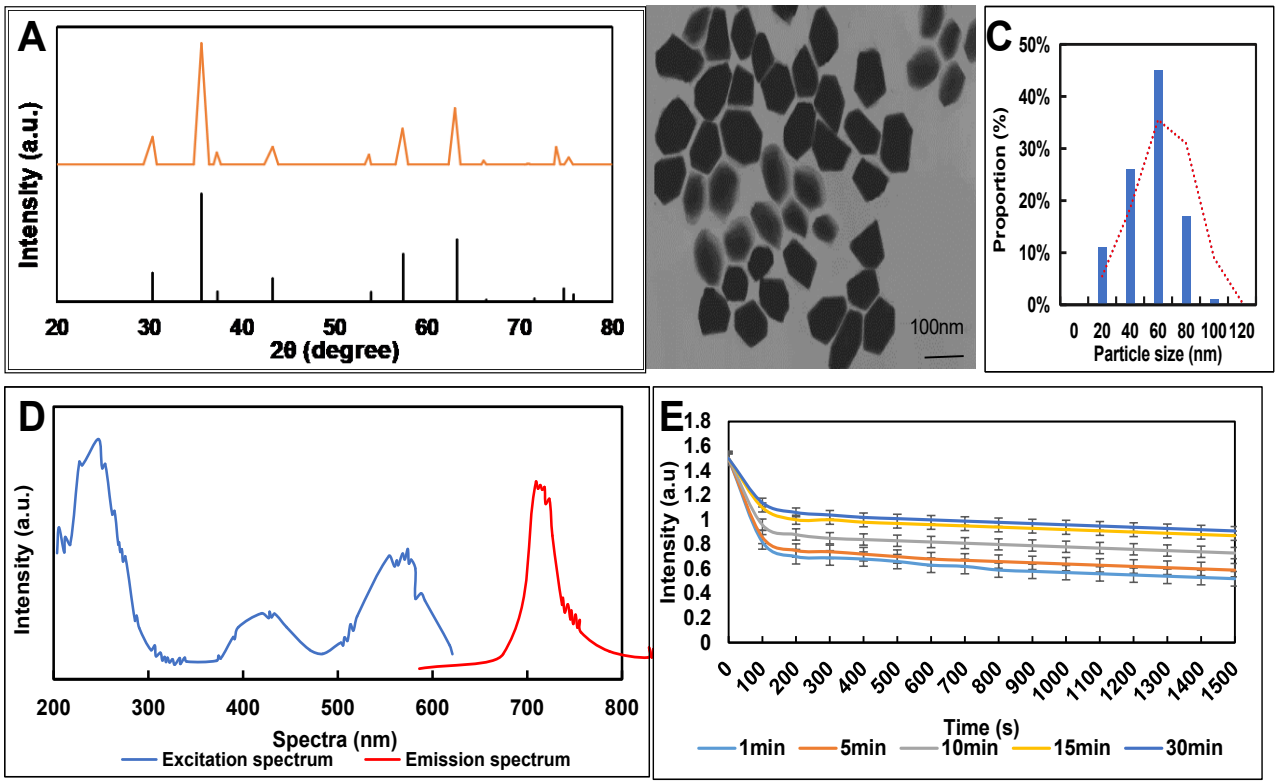

Figure 1: Characterization analysis result. A: X-ray diffraction pattern; B: electron microscopic observation; C: particle size distribution; D: fluorescence spectrum analysis; E: attenuation curve of nanomaterials.

Effect of thermal treatment temperature on nanomaterials: When the thermal treatment temperature was 800°C,$ZnGa_2O_4:Cr^{3+}$NIR nanomaterialssize was mostly in the range of 40~60nm and was relatively well-dispersed. When the thermal treatment temperature was 1,200°C, $ZnGa_2O_4:Cr^{3+}$NIR nanomaterials size was mostly around 100 nm, but severe agglomeration occurred, resulting in uneven distribution. In comparison with $ZnGa_2O_4:Cr^{3+}$NIR nanomaterialsprepared at a

thermal treatment temperature of 1,000°C, it was evident that 1,000°C was more suitable (Figure 2A-D).

The afterglow performance of the samples prepared at different thermal treatment temperatures was also analyzed, and the results revealed that with increasing temperature, the initial afterglow intensity of the samples increased, and the decay rate gradually decreased (Figure 2E).

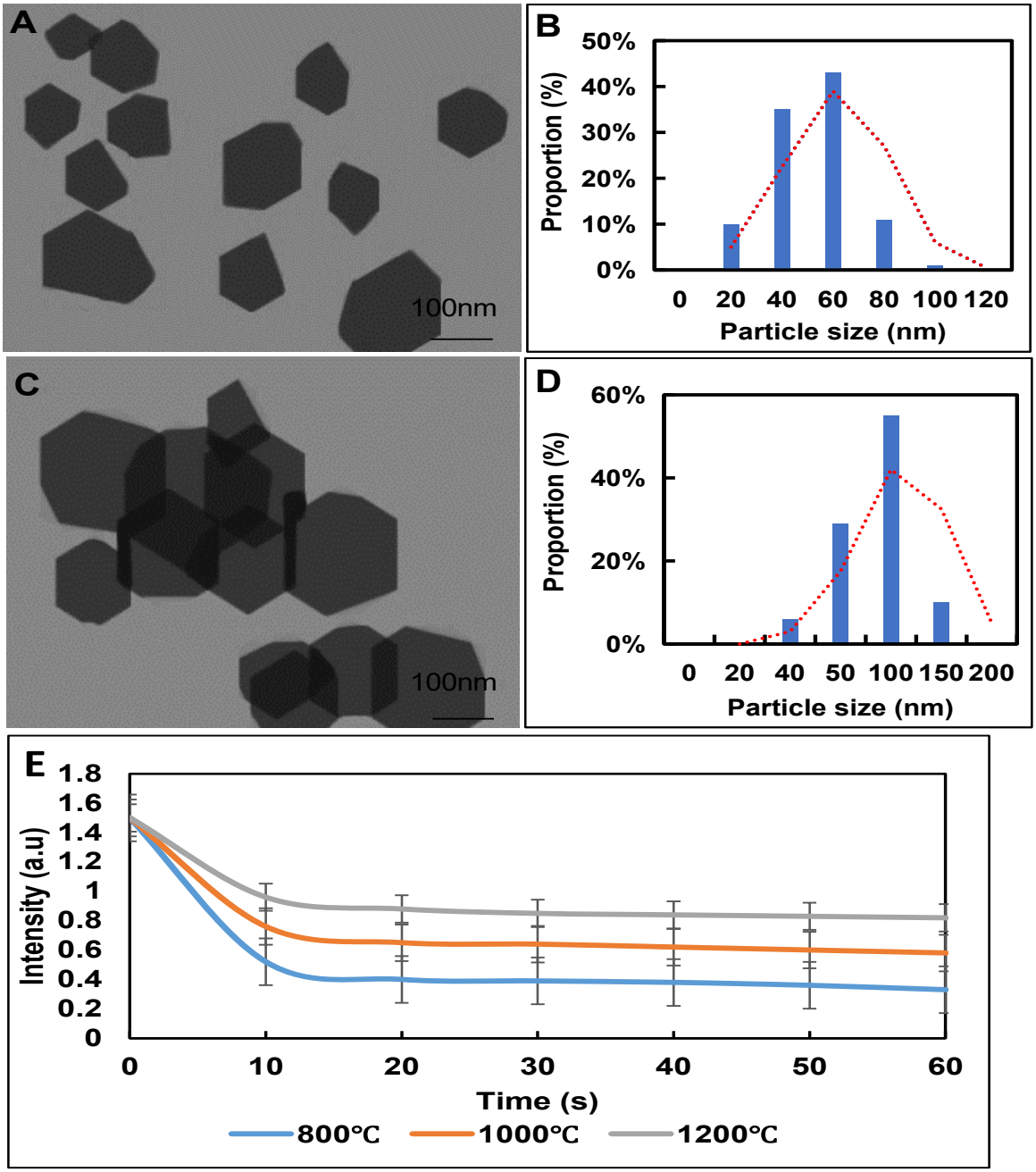

Figure 2: Observation results of $ZnGa_2O_4:Cr^{3+}$NIR nanomaterials characterization at different thermal treatment temperatures. A, B: 800°C; C, D: 1,200°C; E: After glow attenuation curves at different thermal treatment temperatures.

Verification results of rat model: According to pathological HE staining, it was observed that there was no inflammatory response in the brain tissue of the rats in control group; in contrast, the brain tissue of rats in experimental group exhibited extensive infiltration of inflammatory cells, vasodilation, and granuloma

formation (Figure 3).Quantitative analysis showed that the inflammatory cells count in experimental group was 48.3 ± 6.7 cells/field (400×), significantly higher than the 16.2 ± 1.5 cells/field in control group(P<0.05). Histological scoring revealed an average score of 0.5 ± 0.3 for control group, the score for the rats in experimental group was 3.7 ± 0.5 (P<0.05), further confirming the successful establishment of the tuberculous meningitis model.

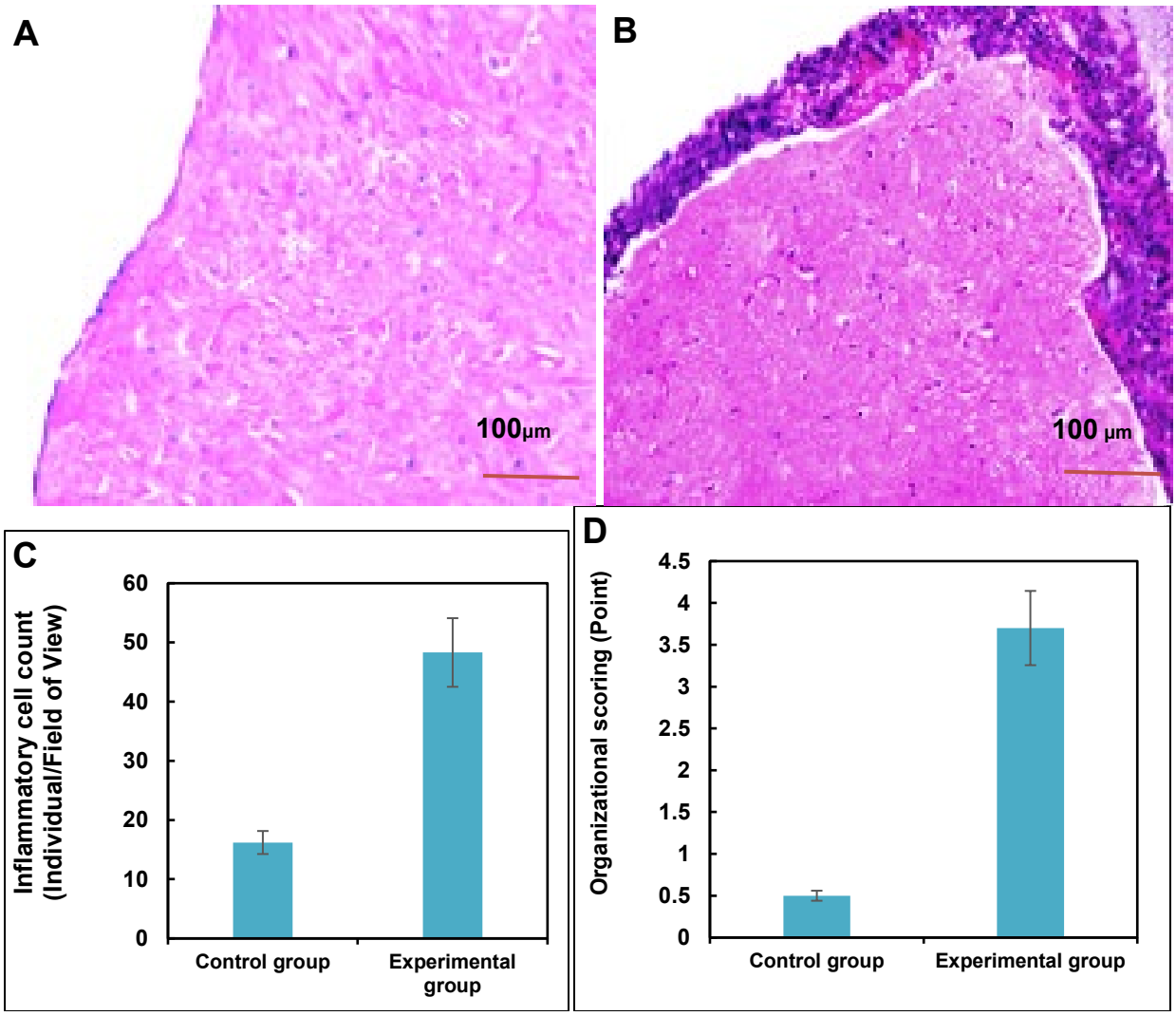

Figure 3:HE staining results (×400). A: control group; B:experimental group. C: inflammatory cell count; D: organizational scoring.

Analysis of *in vivo* imaging results: The optical imaging results indicated that at 1 minute of imaging, there was a strong signal observed in the rat's head. Even after 30 minutes of imaging, although the signal intensity slightly decreased, it remained strong (Figure 4A).MRI images further revealed mild thickening of the meninges in rat basal cistern, nodular ring enhancement, and a small amount of ventricular hydrocephalus (Figure 4B-C). Quantitative analysis showed that MRI signal intensity in $ZnGa_2O_4$:Cr^{3+}NIR group was significantly higher than that in saline group. The signal-to-noise ratio increased from 4.5 ± 0.8 in the saline group to 8.2 ± 1.2 in $ZnGa_2O_4$:Cr^{3+}NIR group (P<0.05). Additionally, the contrast-to-noise ratio for $ZnGa_2O_4$:Cr^{3+}NIR group was 3.5 ± 0.6, compared to 1.9 ± 0.4 in saline group (P<0.05). The ventricular area in $ZnGa_2O_4$:Cr^{3+}NIRgroup was 0.38 ± 0.05 cm^2, compared to 0.45 ± 0.06 cm^2 in saline group (P<0.05), representing an approximately 15% reduction in ventricular area (Table 2).

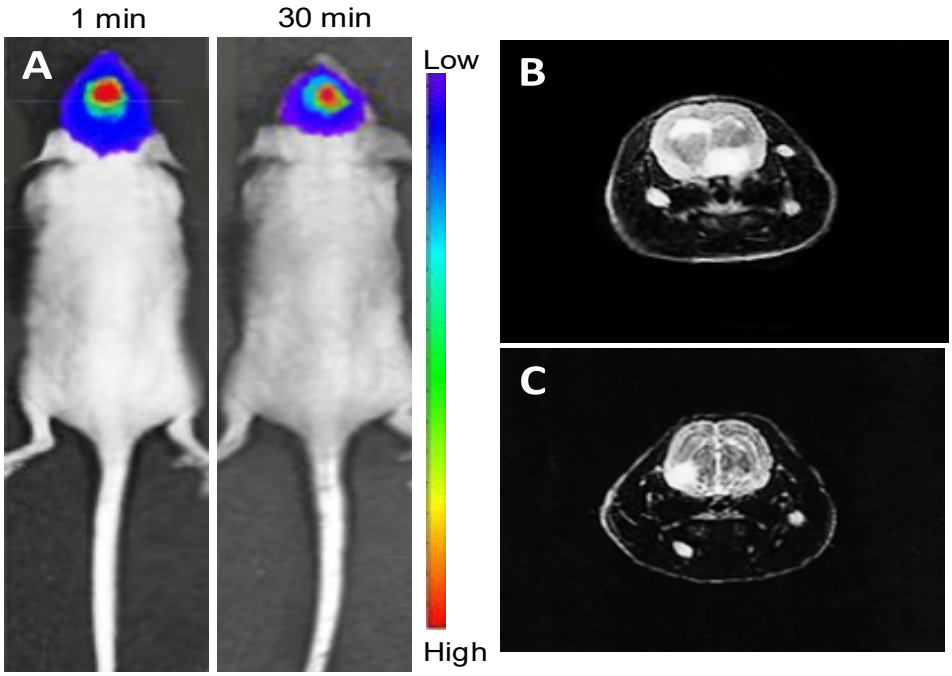

Figure 4: NIR optical imaging and MRI results. A: NIR optical imaging; B: MRI results of saline group; C: MRI results of $ZnGa_2O_4:Cr^{3+}$NIR group.

Table 2.The quantitative assessment results of MRI imaging parameters in the two groups of rats.

Group	Signal-to-noise ratio	Contrast-to-noise ratio	Ventricular Area (cm^2)	Ventricular area change (%)
Saline group (n=2)	4.5 ± 0.8	1.9 ± 0.4	0.45 ± 0.06	-
$ZnGa_2O_4:Cr^{3+}$NIR group(n=2)	8.2 ± 1.2	3.5 ± 0.6	0.38 ± 0.05	-15%
t	8.32	7.45	9.87	-
P	0.023	0.033	0.021	-

DISCUSSION

The crystal structure of nanomaterials plays a crucial role in their properties and adoptions. Thisresearchfound that the XRD diffraction peaks of the prepared NIRlong afterglow nanomaterials were in good agreement with the standard card, indicating that the synthesized nanomaterials possess good structural stability, thus laying a foundation for subsequent experiments. However, the effects of Cr^{3+} doping still require further investigation. Although the XRD results did not show significant structural changes, doping may potentially improve the photoluminescent properties and other characteristics of the material. Therefore, future studies should further examine the impact of doping concentration on material properties, particularly with respect to crystal structure changes under varying doping concentrations. Zheng *et al.* also explored the effect of different doping concentrations of luminescent centers on long afterglow nanomaterials, yielding promising results (Zheng *et al.,* 2020). Future research can further validate these findings and explore optimization strategies for doping. Future research in this aspect could further validate the findings. The near-circular irregular polygonal shape may be attributed to the control conditions during the preparation process and the minimization of surface energy effects. In addition, TEM images showed that the particle size was primarily distributed around 60 nm, with good dispersion, which is consistent with previous studies (Li *et al.,* 2019; Wang *et al.,* 2021; Tang *et al.,* 2022). Although these sizes are considered suitable for biological absorption, the effect of particle size on biological uptake still requires further investigation, especially with regard to the distribution, penetration ability, and potential size-dependent toxicity of different-sized particles within cells. Studies noted that the size of nanoparticles directly affects their *in vivo* biodistribution, uptake efficiency, and toxicity (Li *et al.,* 2019). Therefore, a systematic evaluation of the biocompatibility and toxicity of particles within these size ranges is necessary to ensure their safety. The NIR region refers to the longer wavelength region of the

electromagnetic spectrum beyond the red light of the visible spectrum, with a wavelength range of approximately 700 to 900 nm (Musa *et al.*, 2022). NIR light possesses high penetration ability, enabling it to propagate through biological tissues with minimal absorption or scattering by the tissues. The NIR emission peak of approximately 709 nm for the prepared NIR luminescent persistent nanomaterial falls within the NIR region, indicating favorable penetration within biological tissues, which provides higher imaging depth and lower tissue scattering, making it suitable for subsequent investigations. Similar research by Yu *et al.*, (2022) also demonstrated the broad adoption prospects of up-conversion nanoparticles as NIR nanoprobes for sensitive and deep tissue detection of ROS/RNS.At the same time, thisresearch found that the decay curve of the prepared NIRafterglow nanomaterials exhibited a "fast initial decrease followed by a slow plateau" trend under different excitation times. The rapid initial decay rate may be attributed to non-radiative losses of photons and surface states (Lin *et al.*, 2016). As time progresses, the decay rate gradually slowed down, possibly due to the interaction between photons inside the nanomaterial and processes such as reflection, scattering, and re-excitation within the material (Koe *et al.*, 2020). Within the excitation time range of 15 to 30 minutes, the afterglow performance became consistent, indicating that the nanomaterials exhibited high and stable luminescent intensity during this period. However, it is important to note that extending the excitation time may increase the risk of photodamage to biological tissues. Extended excitation could potentially induce phototoxicity, affecting the health and function of cells or tissues. To balance luminescence intensity with the safety of experimental organisms and their tissues, 15 minutes was selected as the optimal excitation time to ensure that the nanomaterials provide sufficient luminescent intensity without significantly increasing photodamage. Furthermore, future studies should further assess the potential phototoxic effects of different excitation times on biological tissues, particularly in cell or small animal model experiments, to ensure their safety in practical applications.

In the preparation of luminescent nanomaterials using the sol-gel method, thermal treatment is necessary. Previous literature has indicated that after thermal treatment, the nanoparticles tend to agglomerate, leading to an increase in particle size (Ren *et al.*, 2022; Zhang *et al.*, 2021; Niu *et al.*, 2021). Hence, further analysis was conducted on the NIR afterglow nanomaterials prepared at various thermal treatment temperatures. $ZnGa_2O_4:Cr^{3+}$NIR nanomaterials prepared at 800°C exhibited smaller and more dispersed particles, attributed to the slow grain growth at lower thermal treatment temperatures, resulting in smaller particles. At 1,200°C, the particle size increased greatly and severe agglomeration occurred, likely due to accelerated aggregation and crystal growth at high temperatures. Relatively speaking, a thermal treatment temperature of 1,000°C allowed better control of crystal growth and aggregation of the nanomaterials, facilitating the production of more uniformly sized nanoparticles. However, some slight aggregation phenomena were still observed in the TEM images, which may be attributed to the enhanced van der Waals or electrostatic forces between particles at high temperatures, leading to minor particle agglomeration. Additionally, the inherent inhomogeneity during the crystal growth process and natural fluctuations in the particle size distribution could also contribute to the aggregation of certain particles. Nonetheless, the heat treatment temperature of 1,000°C was still effective in controlling particle size and enhancing the optical performance of the nanomaterials. Based on previous literature, materials require high-temperature treatment to increase the quantity and depth of traps, which enhances the afterglow emission performance of nanomaterials during this process (Ding *et al.*, 2023; Liu *et al.*, 2022). Hence, the afterglow performance of the nanomaterials prepared at different thermal treatment temperatures was analyzed. As the thermal treatment temperature increased, the initial afterglow intensity of $ZnGa_2O_4:Cr^{3+}$NIR nanomaterialsenhanced. This is likely due to the high-temperature treatment facilitating the formation or activation of luminescent centers within the material, thereby increasing the luminescence efficiency. Furthermore, as the temperature increased, the decay rate of the afterglow in $ZnGa_2O_4:Cr^{3+}$NIR nanomaterialsgradually decreased. This effect may be attributed to the high-temperature treatment improving the crystallinity and crystal defects of the material, consequently reducing non-radiative energy loss and interactions between photons and the material.

To further verify the MRI*in vivo* imaging effect of NIR luminescent afterglow nanomaterials used in rat model of tuberculous meningitis, a rat model of tuberculous meningitis was first prepared by injecting tuberculosis bacteria. HE staining results showed that the brain tissue of rat model showed many inflammatory cell infiltration, vascular dilation, and granuloma formation, which are typical pathological changes of tuberculous meningitis (Schaller *et al.*, 2019), indicating that we had successfully prepared a rat model of tuberculous meningitis, which can be used for subsequent experiments. Quantitative analysis results further revealed that, after the injection of NIRpersistent luminescence nanomaterials, the signal intensity and contrast in rat MRI imaging were significantly improved. The signal-to-noise ratio increased from 4.5±0.8 to 8.2±1.2 (P<0.05), and the contrast-to-noise ratio rose from 1.9±0.4 to 3.5±0.6 (P<0.05). Additionally, the ventricular area decreased from 0.45±0.06 cm^2 to

0.38±0.05 cm^2 (P<0.05), representing a reduction of approximately 15%. These results indicate that the nanomaterials effectively enhanced the quality of MRI imaging and improved the imaging characteristics of hydrocephalus, demonstrating their potential as MRI contrast agents in a tuberculous meningitis model. The injection of these nanomaterials may function as a contrast agent, interacting with MRI contrast agents through their unique optical and magnetic properties, thereby improving image contrast and resolution. Specifically, the NIRpersistent luminescence nanomaterials emit light in the NIRregion, extending the signal decay time, which helps reduce background noise and enhances image clarity and contrast. Furthermore, the magnetic properties of these nanomaterials may interact with the physical mechanisms of MRI, altering magnetic field effects, which in turn enhances MRI signal strength and spatial resolution. The unique optical characteristics of these nanomaterials can also provide additional signal enhancement through the light excitation process, improving image quality. This multifaceted physicochemical interaction mechanism could significantly contribute to the enhancement of MRI imaging quality. Liu *et al.*, (2019) demonstrated the ultra-sensitive detection and inhibition of breast cancer cell metastasis to nearby lymph nodes and distant organs using long-lasting luminescent nanoparticles. Their results indicated that background-free NIR long persistent luminescence (NIR-PL) imaging exhibited higher sensitivity compared to classical bioluminescence imaging. Pei*et al.*, (2021) applied NIR luminescent nanoparticles to multi-modal MRI and positron emission tomography imaging of mouse tumors, showing a four-fold increase in signal-to-noise ratio and a three-fold improvement in imaging clarity. These findings are consistent with the results of this research. However, previous research on the adoption of luminescent long-afterglow nanomaterials in MRI is limited, and further investigations are needed to confirm the safety of NIR luminescent long-afterglow nanomaterials in biological systems.

However, this research has some limitations. Firstly, further in-depth research is required to assess the biocompatibility and toxicity of NIR luminescent long-afterglow nanomaterials. Although *in vivo*MRI imaging results of rats' brains were obtained under experimental conditions, the feasibility and efficacy in clinical adoptions still need further validation. Additionally, there is a need for further research on the optimization of nanomaterial properties, imaging parameters, and dosage control. Comparative studies of different preparation methodologies can also be explored to enhance biocompatibility and luminescence performance of nanomaterials.

Conclusion: This study confirmed the application of $ZnGa_2O_4:Cr^{3+}$NIR persistent luminescence nanomaterials in MRI imaging of tuberculous meningitis in rats. The material demonstrates excellent luminescent properties and stable decay performance, significantly enhancing the resolution and contrast of MRI, and effectively amplifying the signals of brain lesions. This provides a novel technical approach for imaging neurological diseases.

Funding information: None.

Author contributions: Xiaoyu Li: data analysis, experiments carried out; Xiaoyu Li andLiyingzi Huang: data interpretation, data analysis, methodology, and review of manuscript; Xiaoyu Li andLiyingzi Huang: study concept, design, supervision, and proofreading of the manuscript.

Animal rights statement: The animal experiments strictly adhered to the guidelines for experimental procedures and ethical principles to ensure scientific validity, reliability, and respect for animal welfare. The protocols and procedures were approved by the Ethics Committee of theFirst Hospital of Changsha.

Conflict of interests: None.

REFERENCES

Bystritsky, R.J. andF.C.Chow (2022). Infectious meningitis and encephalitis. Neurol. Clin.40(1):77-91. https://doi.org/10.1016/j.ncl.2021.08.006

Biegger, P., M.E. Ladd and D.Komljenovic(2020). Multifunctional magnetic resonance imaging probes. Recent Results Cancer Res.216:189-226. https://doi.org/10.1007/978-3-030-42618-7_6

Chen, L.J., X. ZhaoandX.P. Yan (2019). Cell-penetrating peptide-functionalized persistent luminescence nanoparticles for tracking J774A.1 macrophages homing to inflamed tissues. ACS Appl. Mater. Interfaces.11(22):19894-19901. https://doi.org/10.1021/acsami.9b05870

Dian, S., R. Hermawan, A. van Laarhoven, S. Immaculata, T.H. Achmad, R.Ruslami, F.Anwary, R.D.Soetikno, A.R.GaniemandR.van Crevel(2020). Brain MRI findings in relation to clinical characteristics and outcome of tuberculous meningitis. PLoS One.15(11):e0241974. https://doi.org/10.1371/journal.pone.0241974

Ding, X., Y. Min, C. Wang and Q. Zhang (2023). Near-infrared emission material with superlong afterglow performance and its multifunctional applications. Inorg. Chem.62(4):1686-1696. https://doi.org/10.1021/acs.inorgchem.2c04112

Fukushima, S., K. Ocho, K. Fujita, H. Hagiya and F. Otsuka (2023). Tuberculous meningitis. Clin. Case Rep. 11(1):e6865. https://doi.org/10.1002/ccr3.6865

Ge, K., J. Liu, P. Wang, G. Fang, D. Zhang and S. Wang (2019). Near-infrared-emitting persistent luminescent nanoparticles modified with gold nanorods as multifunctional probes for detection of arsenic(III). Mikrochim Acta.186(3):197. https://doi.org/10.1007/s00604-019-3294-z

Clément, S. and A.Mehdi (2020). Sol-Gel Chemistry: from molecule to functional materials. Molecules.25(11):2538. https://doi.org/10.3390/molecules25112538

Iannucci, J., R. Dominy, S. Bandopadhyay, E.M. Arthur, B.Noarbe, A.Jullienne, M.Krkasharyan, R.P. Tobin, A. Pereverzev, S. Beevers, L.Venkatasamy, K.A. Souza, D.C.Jupiter, A. Dabney, A. Obenaus, M.K. Newell-Rogers and L.A. Shapiro (2024). Traumatic brain injury alters the effects of class II invariant peptide (CLIP) antagonism on chronic meningeal CLIP + B cells, neuropathology, and neurobehavioral impairment in 5xFAD mice. J. Neuroinflammation.21(1):165. https://doi.org/10.1186/s12974-024-03146-z

Jacob, L., J. de Brito Neto, S. Lenck, C. Corcy, F.Benbelkacem, L.H. Geraldo, Y. Xu, J.M.Thomas, M.R. El Kamouh, M.Spajer, M.C. Potier, S. Haik, M.Kalamarides, B.Stankoff, S.Lehericy, A. Eichmann and J.L. Thomas (2022). Conserved meningeal lymphatic drainage circuits in mice and humans. J. Exp. Med.219(8):e20220035. https://doi.org/10.1084/jem.20220035

Jiang, Y., J. Huang, X. Zhen, Z. Zeng, J. Li, C. Xie, Q. Miao, J. Chen, P. Chen and K. Pu (2019). A generic approach towards afterglow luminescent nanoparticles for ultrasensitive in vivo imaging. Nat Commun.10(1):2064. https://doi.org/10.1038/s41467-019-10119-x

Koe, W.S., J.W. Lee, W.C. Chong, Y.L. Pang and L.C.Sim (2020). An overview of photocatalytic degradation: photocatalysts, mechanisms, and development of photocatalytic membrane. Environ. Sci. Pollut. Res. Int.27(3):2522-2565. https://doi.org/10.1007/s11356-019-07193-5

Liu, H., R. Chen, C. Tong and X.W.Liang (2021). MRI versus CT for the detection of pulmonary nodules: a meta-analysis. Medicine (Baltimore).100(42):e27270. https://doi.org/10.1097/MD.0000000000027270

Liu, H., F. Ren, X. Zhou, C. Ma, T. Wang, H. Zhang, Q. Sun and Z.Li (2019). Ultra-sensitive detection and inhibition of the metastasis of breast cancer cells to adjacent lymph nodes and distant organs by using long-persistent luminescence nanoparticles. Anal Chem.91(23):15064-15072. https://doi.org/10.1021/acs.analchem.9b03739

Liu, Y., Z. Wang, K. Miao, X. Zhang, W. Li, P. Zhao, P. Sun, T. Zheng, X. Zhang andC.Chen (2022). Research progress on near-infrared long persistent phosphor materials in biomedical applications. Nanoscale Adv.4(23):4972-4996. https://doi.org/10.1039/d2na00426g

Lin, H., L. Zhu, H. Huang, C.J.Reckmeier, C. Liang, A.L.Rogach and W.C.Choy (2016). Efficient near-infrared light-emitting diodes based on organometallic halide perovskite-poly(2-ethyl-2-oxazoline) nanocomposite thin films. Nanoscale.8(47):19846-19852. https://doi.org/10.1039/c6nr08195a

Li, Q., J. Zeng, Q. Miao and M. Gao (2019). Self-Illuminating agents for deep-tissue optical imaging. Front. BioengBiotechnol.7:326. https://doi.org/10.3389/fbioe.2019.00326

Méchaï, F. and O.Bouchaud(2019). Tuberculous meningitis: challenges in diagnosis and management. Rev. Neurol (Paris).175(7-8):451-457. https://doi.org/10.1016/j.neurol.2019.07.007

Mekonnen, T.W., Y.S. Birhan, A.T.Andrgie, E.Y.Hanurry, H.F. Darge, H.Y. Chou, J.Y. Lai, H.C. Tsai, J.M. Yang and Y.H. Chang (2019). Encapsulation of gadolinium ferrite nanoparticle in generation 4.5 poly(amidoamine) dendrimer for cancer theranostics applications using low frequency alternating magnetic field. Colloids Surf B Biointerfaces.184:110531. https://doi.org/10.1016/j.colsurfb.2019.110531

Mahata, M.K., R. De and K.T. Lee (2021). Near-infrared-triggered upconverting nanoparticles for biomedicine applications. Biomedicines.9(7):756. https://doi.org/10.3390/biomedicines9070756

Musa, A., M.L. Hakim, T. Alam, M.T. Islam, A.S. Alshammari, K. Mat, M.S. M, S.H.A.Almalki and M.S. Islam (2022). Polarization independent metamaterial absorber with anti-reflection coating nanoarchitectonics for visible and infrared window applications. Materials (Basel).15(10):3733. https://doi.org/10.3390/ma15103733

Manyelo, C.M., R.S. Solomons, G.Walzl and N.N.Chegou(2022). Tuberculous meningitis: pathogenesis, immune responses, diagnostic challenges, and the potential of biomarker-based approaches. J. Clin. Microbiol.59(3):e01771-20. https://doi.org/10.1128/JCM.01771-20

Niu, F., D. Hu, F. Gu, Y. Du, B. Zhang, S. Ma and W. Pan (2021). Preparation of ultra-long stable ovalbumin/sodium carboxymethylcellulose

nanoparticle and loading properties of curcumin. Carbohydr Polym.271:118451. https://doi.org/10.1016/j.carbpol.2021.118451

Pei, P., Y. Chen, C. Sun, Y. Fan, Y.Yang, X. Liu, L. Lu, M. Zhao, H. Zhang, D. Zhao, X.Liu and F. Zhang (2021). X-ray-activated persistent luminescence nanomaterials for NIR-II imaging. Nat. Nanotechnol.16(9):1011-1018. https://doi.org/10.1038/s41565-021-00922-3

Ren, Z., Z. Chen, Y. Zhang, X. Lin, W. Weng, G. Liu and B.Li (2022). Characteristics of Pickering emulsions stabilized by tea water-insoluble protein nanoparticles at different pH values. Food Chem.375:131795. https://doi.org/10.1016/j.foodchem.2021.131795

Schraven, S., R. Brück, S.Rosenhain, T.Lemainque, D. Heines, H.Noormohammadian, O.Pabst, W. Lederle, F.Gremse and F. Kiessling (2024). CT- and MRI-aided fluorescence tomography reconstructions for biodistribution analysis. Invest Radiol.59(7):504-512. https://doi.org/10.1097/RLI.0000000000001052

Saeboe, A.M., A.Y. Nikiforov, R.Toufanian, J.C. Kays, M. Chern, J.P. Casas, K. Han, A.Piryatinski, D. Jones and A.M. Dennis (2021). Extending the near-infrared emission range of indium phosphide quantum dots for multiplexed. In Vivo Imaging. Nano Lett.21(7):3271-3279. https://doi.org/10.1021/acs.nanolett.1c00600

Schaller, M.A., F. Wicke, C. Foerch andS.Weidauer (2019). Central nervous system tuberculosis: etiology, clinical manifestations and neuroradiological features. Clin. Neuroradiol.29(1):3-18. https://doi.org/10.1007/s00062-018-0726-9

Tang, B., W. Xia, W. Cai and J. Liu (2022). Luminescent gold nanoparticles with controllable hydrophobic interactions. Nano Lett.22(20):8109-8114. https://doi.org/10.1021/acs.nanolett.2c02486

Wang, Y., H.M. Meng and Z. Li (2021). Near-infrared inorganic nanomaterial-based nanosystems for photothermal therapy. Nanoscale.13(19):8751-8772. https://doi.org/10.1039/d1nr00323b

Yu, X., W. Ouyang, H. Qiu, Z. Zhang, Z. Wang and B. Xing (2022). Detection of reactive oxygen and nitrogen species by upconversion nanoparticle-based near-infrared nanoprobes: recent progress and perspectives. Chemistry. 28(65):e202201966. https://doi.org/10.1002/chem.202201966

Yang, Y., T. Yang, F. Chen, C. Zhang, B. Yin, X. Yin, L. Han, Q. Xie, X.B. Zhang andG.Song (2022). Degradable magnetic nanoplatform with hydroxide ions triggered photoacoustic, mr imaging, and photothermal conversion for precise cancer theranostic. Nano Lett.22(8):3228-3235. https://doi.org/10.1021/acs.nanolett.1c04804

Zhang, C., X. Gao, W. Chen, M. He, Y. Yu, G. Gao andT.Sun (2022). Advances of gold nanoclusters for bioimaging. iScience.25(10):105022. https://doi.org/10.1016/j.isci.2022.105022

Zhang, D., F. Jiang, J. Ling, X.K. Ouyang and Y.G.Wang (2021). Delivery of curcumin using a zein-xanthan gum nanocomplex: Fabrication, characterization, and in vitro release properties. Colloids Surf B Biointerfaces.204:111827. https://doi.org/10.1016/j.colsurfb.2021.111827

Zhang, X.H. and H.M.Liang (2019). Systematic review with network meta-analysis: Diagnostic values of ultrasonography, computed tomography, and magnetic resonance imaging in patients with ischemic stroke. Medicine (Baltimore).98(30):e16360. https://doi.org/10.1097/MD.0000000000016360

Zheng, S., J.Shi, X. Fu, C. Wang, X. Sun, C. Chen, Y. Zhuang, X. Zou, Y. Li andH.Zhang (2020). X-ray recharged long afterglow luminescent nanoparticles MgGeO3:Mn2+,Yb3+,Li+ in the first and second biological windows for long-term bioimaging. Nanoscale.12(26):14037-14046. https://doi.org/10.1039/c9nr10622g

Zhao, X., L. Zhang, X. Yan, L. Zhang, Y. Lu, J. Pan, M. Zhang, C. Wang, H. Suo, X. Jia, X. Liu and G. Lu (2021). A near-infrared light triggered fluormetric biosensor for sensitive detection of acetylcholinesterase activity based on NaErF4: 0.5 % Ho3+@NaYF4 upconversion nano-probe. Talanta.235:122784. https://doi.org/10.1016/j.talanta.2021.122784.